Load-Mismatch Tracking Digital Predistortion Technique for Mobile-Terminal Power Amplifiers

Xin Liu, *Member, IEEE*, Wenhua Chen, *Senior Member, IEEE*, Wenhao Chen, Yan Guo, and Zhenghe Feng, *Life Fellow, IEEE*

***Abstract*— The power amplifiers (PAs) often suffer from load mismatch in mobile terminals due to the complicated working environments, making linearizing those PAs a challenging task. This article proposes a novel load-mismatch tracking digital predistortion (LMT-DPD) technique for linearizing mobile-terminal PAs under varying load-mismatch conditions. The time-domain polyharmonic distortion (TD-PHD) model is discussed first for the behavioral modeling and linearization of PA under mismatch, followed by a practical model construction method. Then, the proposed LMT-DPD technique is derived based on the superposition principle. According to the real-time load reflection coefficients, the LMT-DPD enables automatic and fast adjustments of the predistorter to adapt to the PA's nonlinear distortion under different load-mismatch conditions without coefficient recalibration. Experimental validations are carried out on a mobile-terminal PA module at 4.6 GHz with a 100-MHz 5G new radio (NR) signal. The test results show that the proposed LMT-DPD technique can significantly reduce the update frequency of predistorter while realizing excellent linearization performance.**

***Index Terms*— Digital predistortion, load mismatch, mobile terminal, power amplifiers (PAs), time-domain polyharmonic distortion (TD-PHD) model.**

I. Introduction

MODERN communication systems are continuously evolving to fulfill the growing users' demand for faster transmission rate and data capacity, leading to broader signal bandwidth, high-order modulations, and high peak-to-average power ratio (PAPR). The requirements for the linearity of the transmission signal are more stringent, and higher energy efficiency of transmitters is essential for the designers to achieve green communication [1].

The power amplifiers (PAs) are the most power-hungry components in radio frequency (RF) front ends, and their efficiency will directly affect the performance of the transmitters [2]. However, the PAs will suffer from strong nonlinear distortion when delivering high efficiency. Additional linearization techniques are usually adopted in transmitters to address the PAs' conflict between efficiency and linearity [3]. Currently, digital predistortion (DPD) is one of the most popular linearization techniques in modern wireless communication systems [4], [5].

Based on accurate behavioral modeling, DPD can predict the nonlinear distortion of the PA and eliminate it by adding a proper predistorted signal [5], [6], [7], [8]. Fig. 1 shows the structure of a typical DPD system, which contains a predistorter, a model identification module, and a feedback loop [9]. The predistorter will generate the DPD signal in real time, and its coefficients should be updated to adapt to the amplifier's operating status. Therefore, a model identification module is necessary, which will be activated frequently to extract the model's coefficients with the PA's input and output signals.

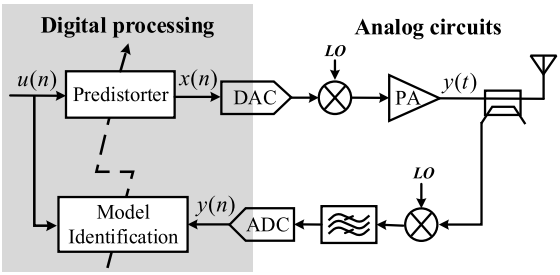

Fig. 1. Block diagram of the typical DPD system.

Traditional DPD studies mainly focus on its application in high-power base stations [10], [11], [12], [13]. In base station equipment, an isolator is inserted between the PA and the antenna to stabilize the amplifier's output impedance. However, limited by the hardware cost and volume budget, the bulky isolators are usually removed in 5G mobile handsets [14]. Therefore, mobile-terminal PAs are sensitive to the variation of the antenna impedance, which frequently occurs since the reflection objects close to the antenna change quickly as the terminal device moves around [15]. When the impedance of the antenna derivates from 50 Ω, the PA will suffer from load mismatch [16]. This mismatch will induce an unexpected reflective wave at the PA's output, resulting

Manuscript received 9 July 2022; revised 6 November 2022; accepted 19 November 2022. Date of publication 2 December 2022; date of current version 13 January 2023. This work was supported in part by the National Key Research and Development Program of China under Grant 2018YFB1802104 and Grant 2018YFB1801600, in part by the National Natural Science Foundation of China under Grant 61941103 and Grant 62101411, in part by the National Key Research and Development Program of Hebei Province under Grant 20310401D, in part by the China Post-Doctoral Science Foundation under Grant 2019M663930XB, in part by the Science and Technology Major Project of Shaanxi Province under Grant 2020zdzx05-01-01, and in part by the Beijing National Research Center for Information Science and Technology (BNRist). This article is an expanded version from the IEEE MTT-S International Microwave Symposium (IMS 2022), Denver, CO, USA, June 19–24, 2022 [DOI: 10.1109/IMS37962.2022.9865494]. *(Corresponding author: Xin Liu.)*

Xin Liu is with the Key Laboratory of Wide Bandgap Semiconductor Technology, School of Microelectronics, Xidian University, Xi'an 710071, China (e-mail: liuxin01@xidian.edu.cn).

Wenhua Chen and Zhenghe Feng are with the Department of Electronic Engineering, Tsinghua University, Beijing 100084, China.

Wenhao Chen and Yan Guo are with Huawei Technologies Company Ltd., Shanghai 200121, China.

Color versions of one or more figures in this article are available at https://doi.org/10.1109/TMTT.2022.3224738.

Digital Object Identifier 10.1109/TMTT.2022.3224738

in overall performance degradation, including more severe nonlinear distortions, reduced output power and efficiency, and poorer stability [17], [18], [19], [20]. The PA's working status and nonlinear characteristics will change with the variation of its load impedance, making it complicated to linearize such a PA. Recently, dealing with the load mismatch of PAs in mobile terminals has become a common concern for researchers in both industry and academia [21], [22], [23], [24], [25].

In wireless mobile terminals, linearization for PAs involves several unique challenges. Specifically, the DPD technique has to track more severe environmental variations than those found in base stations [26]. First, the nonlinear distortions of PA under load mismatch with high-voltage standing wave ratio (VSWR) are different, and DPD is expected to compensate for these "unusual" distortions effectively. Second, since the load impedance may change quickly in mobile terminals, the DPD model must be frequently updated to track the PA's nonlinear behavior in real time.

Behavioral models for PAs under load mismatch have been studied in the literature [27], [28], [29], [30], [31], [32], [33], [34]. Dual-input models considering reflection wave are investigated in [27], [28], [29], [30], [31], and [32]. Zargar et al. [27] derived a double-input–double-output (DIDO) model from the dual-input Volterra series and proposed to extract the model coefficients with the PA's input and output signals under different load conditions. Although the modeling accuracy is satisfied, the complexity is unaffordable for the handsets since the DIDO model contains abundant nonlinear basis functions. Then, Cai et al. [28] simplified the DIDO model and proposed the D-quasi-polyharmonic distortion (QPHD) model. The dc response is also introduced into the dual-input behavioral model in [29] and [30] to enable the prediction of PA's efficiency under load mismatch. In [33], an impedance-dependent MP model (IDMP) is developed by including the load reflection coefficients in the memory polynomial (MP) model. Then, for test conditions, the model coefficients are interpolated from the training sets. Recently, Wang et al. [34] proposed an extended magnitude selective affine (EMAS) model for the behavioral modeling and linearization of the PA under load mismatch, which can achieve significant complexity reduction compared to the conventional generalized MP (GMP) model. Furthermore, a reflection-aware behavioral modeling and DPD method is proposed in [16], which extracts and saves multiple sets of model coefficients for different training load conditions.

Among the literature, we can find that most of the DPD schemes are mainly concerned with the steady-state modeling performance, i.e., which accuracy a model will achieve under a specific mismatch condition. In such a case, the adaption of the DPD model must be triggered repeatedly to track the variation of load mismatch, making the identification complexity unaffordable in mobile terminals.

To resolve this issue, this article proposes a load-mismatch tracking DPD (LMT-DPD) technique. Based on the time-domain polyharmonic distortion (TD-PHD) model, the LMT-DPD technique is derived with the superposition principle. Compared to the conventional adaptive DPD method that recalibrates the DPD coefficients as the load impedance changes, the proposed LMT-DPD technique enables fast and automatic adaption of its coefficients according to the real-time load reflection coefficient without performance degradation. To validate the performance of the LMT-DPD against other DPD update strategies, experimental tests are carried out on a Skyworks sky58255-11 PA module with a 100-MHz 5G new radio (NR) signal.

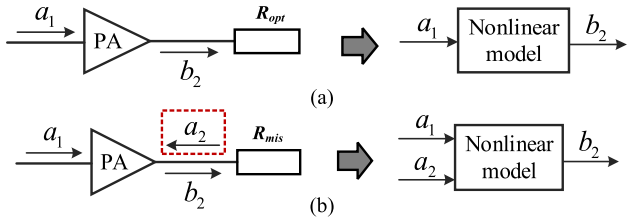

Fig. 2. Behavioral model schematics for PA under (a) load match and (b) load mismatch.

In this article, based on the DPD technique reported in the conference paper [35], more details about the theoretical analysis and methodology of the TD-PHD model and LMT-DPD are presented, as well as a brief discussion about the complexity of the LMT-DPD. The descriptions of the structure of the LMT-DPD are provided in detail, including the actual implementation of the load-mismatch evaluator. In addition, more measurement results, including simulation and experimental results under different PA load conditions, are demonstrated and compared with previous works.

The rest of this article is structured as follows. The TD-PHD model and its construction method are introduced in Section II. Section III provides the details of the proposed LMT-DPD model, including the principle analysis, coefficients extraction method, and working procedures. Section IV gives the simulation and experimental measurement results. A summary will be presented in Section V.

II. TD-PHD Model

Fig. 2 shows the schematics of signal flows when the PA connects to the matched and mismatched load. The input and the output signal are denoted as $a_1(t)$ and $b_2(t)$, respectively. When the PA suffers from load mismatch, a backward incident wave $a_2(t)$ will occur at the output of the amplifier, resulting in more complicated nonlinear distortions. In such a case, the mismatched PA is equivalent to a dual-input nonlinear system, and both the input signal $a_1(t)$ and the reflection signal $a_2(t)$ contribute to the output signal $b_2(t)$, as in the following equation:

$$b_2(t) = G(a_1(t), a_2(t)) \tag{1}$$

where $G(\cdot)$ denotes the nonlinear transfer function of the PA. Note that $a_1(t)$, $a_2(t)$, and $b_2(t)$ only have the fundamental component and memory effect being ignored here. To accurately describe and compensate for the nonlinear distortion of the amplifier under load mismatch, we need to construct a suitable nonlinear transfer function $G(\cdot)$.

The derivation of some basic principles and assumptions in polyharmonic distortion (PHD) modeling theory may be helpful in solving the function $G(a_1(t), a_2(t))$. The PHD modeling is a black-box frequency-domain modeling technique, and it is a natural extension of S-parameters under large-signal conditions [36], [37]. In the derivation of PHD modeling,

an assumption is made that there is only one dominant large-signal input component, while all other input components are relatively small. It is worth noting that the gain normalization of the measured signals is a necessary procedure in the DPD process such that the contributions of the reflection signal $a_2(t)$ on the PA's output is relatively smaller than that of the original input signal $a_1(t)$, though the absolute power of $a_2(t)$ may be larger than the power of $a_1(t)$. Then, the superposition principle can be applied, which assumes that the output response is the superposition of each individual response. From the perspective of behavioral modeling, we can assume that the nonlinear transfer function $G(\cdot)$ is a superposition of three nonlinear functions, as in the following equation:

$$G(a_1(t), a_2(t)) = \varphi_1(a_1(t)) + \varphi_2(a_2(t)) + \varphi_3(a_1(t), a_2(t)) \tag{2}$$

where $\varphi_1(a_1(t))$ and $\varphi_2(a_2(t))$ denote the response imposed by $a_1(t)$ and $a_2(t)$, respectively, while $\varphi_3(a_1(t), a_2(t))$ represents the intermodulation response caused by both $a_1(t)$ and $a_2(t)$.

Since the original input signal $a_1(t)$ is the dominant component that determines the nonlinear response of the amplifier, while the reflection signal $a_2(t)$ is the subordinate component that will impose a small perturbation to the operation of the amplifier around the main operating point [29], [30], it is reasonable to assume that nonlinear responses induced by high-order terms of $a_2(t)$ could be ignored, leading to a simplified $\varphi_2(a_2(t))$ and $\varphi_3(a_1(t), a_2(t))$ as

$$\varphi_2(a_2(t)) \approx g_1 a_2(t) \tag{3}$$

$$\varphi_3(a_1(t), a_2(t)) \approx a_2(t) \cdot \varphi_4(a_1(t)) \tag{4}$$

where g_1 is a constant coefficient and $\varphi_4(a_1(t))$ is a nonlinear function dependent on $a_1(t)$.

Suppose that the nonlinear functions $\varphi_1(a_1(t))$ and $\varphi_4(a_1(t))$ can be approximated by the polynomials, which is also the common case in behavioral modeling, and the function $G(a_1(t), a_2(t))$ has the form (5) when considering the third-order nonlinearity

$$\begin{aligned} b_2(t) &= G(a_1(t), a_2(t)) \\ &\approx \underbrace{c_1 a_1(t) + c_2 a_1^2(t) + c_3 a_1^3(t)}_{\varphi_1(a_1(t))} + \underbrace{g_1 a_2(t)}_{\varphi_2(a_2(t))} \\ &\quad + \underbrace{a_2(t)\big(h_1 a_1(t) + h_2 a_1^2(t)\big)}_{\varphi_3(a_1(t), a_2(t))} \end{aligned} \tag{5}$$

where c_1, c_2, c_3, h_1, and h_2 denote the coefficients of the polynomial.

Assuming that the equivalent complex baseband signals of $a_1(t)$ and $a_2(t)$ are denoted as $\tilde{a}_1(t)$ and $\tilde{a}_2(t)$, respectively, then $a_1(t)$ and $a_2(t)$ are expressed as

$$a_1(t) = \frac{\tilde{a}_1(t)e^{j\omega_c t} + \tilde{a}_1^*(t)e^{-j\omega_c t}}{2} \tag{6}$$

$$a_2(t) = \frac{\tilde{a}_2(t)e^{j\omega_c t} + \tilde{a}_2^*(t)e^{-j\omega_c t}}{2} \tag{7}$$

where $f_c = \omega_c/2\pi$ is the carrier frequency. Substituting (6) and (7) into (5), we can directly obtain (8) with some straightforward derivation

$$\begin{aligned} b_2(t) &= G(a_1(t), a_2(t)) \\ &= \left(\frac{1}{4}h_1\tilde{a}_1^*(t)\tilde{a}_2(t) + \frac{1}{4}h_1\tilde{a}_1(t)\tilde{a}_2^*(t) + \frac{1}{2}c_2|\tilde{a}_1(t)|^2\right) \\ &\quad + \left(\begin{array}{l}\frac{1}{2}c_1\tilde{a}_1(t) + \frac{1}{2}g_1\tilde{a}_2(t) + \frac{3}{8}c_3\tilde{a}_1(t)|\tilde{a}_1(t)|^2 \\ +\frac{1}{4}h_2\tilde{a}_2(t)|\tilde{a}_1(t)|^2 + \frac{1}{8}h_2\tilde{a}_1^2(t)\tilde{a}_2^*(t)\end{array}\right)e^{j\omega_c t} \\ &\quad + \left(\begin{array}{l}\frac{1}{2}c_1\tilde{a}_1^*(t) + \frac{1}{2}g_1\tilde{a}_2^*(t) + \frac{3}{8}c_3\tilde{a}_1^*(t)|\tilde{a}_1(t)|^2 \\ +\frac{1}{4}h_2\tilde{a}_2^*(t)|\tilde{a}_1(t)|^2 + \frac{1}{8}h_2\tilde{a}_1^{*2}(t)\tilde{a}_2(t)\end{array}\right)e^{-j\omega_c t} \\ &\quad + \left(\frac{1}{4}h_1\tilde{a}_1(t)\tilde{a}_2(t) + \frac{1}{4}c_2\tilde{a}_1^2(t)\right)e^{j2\omega_c t} \\ &\quad + \left(\frac{1}{4}h_1\tilde{a}_1^*(t)\tilde{a}_2^*(t) + \frac{1}{4}c_2\tilde{a}_1^{*2}(t)\right)e^{-j2\omega_c t} \\ &\quad + \left(\frac{1}{8}c_3\tilde{a}_1^3(t) + \frac{1}{8}h_2\tilde{a}_1^2(t)\tilde{a}_2(t)\right)e^{j3\omega_c t} \\ &\quad + \left(\frac{1}{8}c_3\tilde{a}_1^{*3}(t) + \frac{1}{8}h_2\tilde{a}_1^{*2}(t)\tilde{a}_2^*(t)\right)e^{-j3\omega_c t}. \end{aligned} \tag{8}$$

Then, if we look at the terms that are proportional to $e^{j\omega_c t}$, the equivalent complex baseband signal of $b_2(t)$ is given as

$$\begin{aligned} \tilde{b}_2(t) = &\frac{1}{2}c_1\tilde{a}_1(t) + \frac{1}{2}g_1\tilde{a}_2(t) + \frac{3}{8}c_3\tilde{a}_1(t)|\tilde{a}_1(t)|^2 \\ &+ \frac{1}{4}h_2\tilde{a}_2(t)|\tilde{a}_1(t)|^2 + \frac{1}{8}h_2\tilde{a}_1^2(t)\tilde{a}_2^*(t). \end{aligned} \tag{9}$$

In actual applications, if the operating point is close to the saturation region, the PA will suffer from severe gain compression and even more complicated nonlinear distortions in broadband scenarios. Hence, (9) should be extended with high-order nonlinearity and memory effect terms, leading to the TD-PHD model in the discrete form [32], [37], as in the following equation:

$$\begin{aligned} \tilde{b}_2(n) = &\sum_{k=1}^{K_1}\sum_{m=0}^{M_1}\alpha_{\mathrm{km}}\tilde{a}_1(n-m)|\tilde{a}_1(n-m)|^{k-1} \\ &+ \sum_{p=0}^{P_1}\beta_p^1\tilde{a}_2(n-p) \\ &+ \sum_{k=2}^{K_2}\sum_{m=0}^{M_2}\sum_{p=0}^{P_2}\beta_{\mathrm{kmp}}^2\tilde{a}_2(n-p)|\tilde{a}_1(n-m)|^{k-1} \\ &+ \sum_{k=1}^{K_3}\sum_{m=0}^{M_3}\sum_{p=0}^{P_3}\gamma_{\mathrm{kmp}}\tilde{a}_1^2(n-m)\tilde{a}_2^*(n-p)|\tilde{a}_1(n-m)|^{k-1} \end{aligned} \tag{10}$$

where α_{km}, β_p^1, β_{kmp}^2, and γ_{kmp} represent the model coefficients. Notably, according to [36] and [37], high-order nonlinearities in (10) can be introduced sufficiently by polynomials of the amplitude of the dominant component, i.e., the input signal $\tilde{a}_1(n)$.

The TD-PHD model is a dual-input model, and both input signal $\tilde{a}_1(n)$ and reflection signal $\tilde{a}_2(n)$ are needed when applying the TD-PHD model. In most existing techniques,

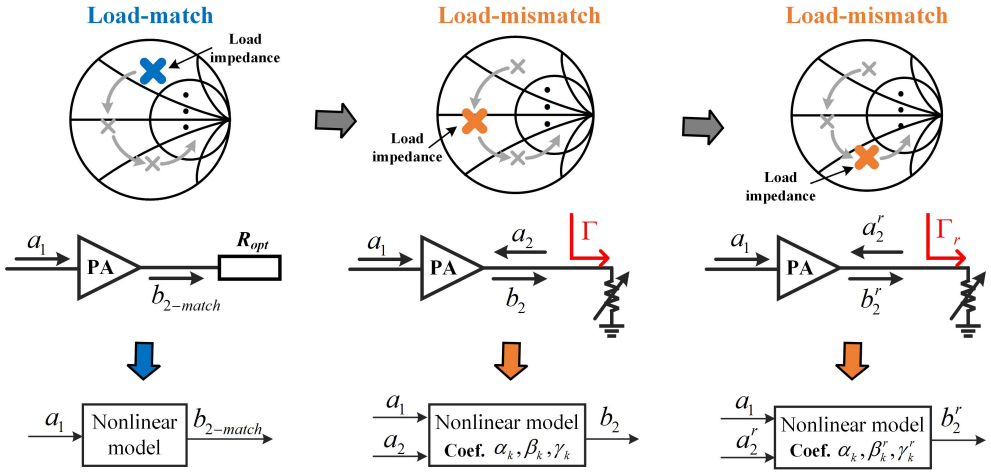

Fig. 3. Schematic of signal flow direction at PA's input and output ports when the load impedance changes.

the reflection signal $\tilde{a}_2(n)$ is obtained by direct measurement at the PA's output, which is practically infeasible in mobile handsets. Here, an alternative method will be introduced in Section III-B to construct $\tilde{a}_2(n)$ without a real-time measurement.

III. Load-Mismatch Tracking DPD Technique

In the DPD technique, the model coefficients of the predistorter should be updated using adaptive identification algorithms such as least squares (LSs) when the PA's nonlinear distortions change obviously. This process will consume a lot of computational resources, especially in mobile terminals where frequent updates of the predistorter are required, while the power budget for the DPD system is limited. In such a case, we propose the LMT-DPD technique to achieve a fast update of the predistorter with low complexity.

A. Methodology

For legibility, the memory terms in the TD-PHD model are ignored in the following derivations.

Fig. 3 shows the diagram of signal flow direction at PA's input and output ports when the load impedance changes. When the PA connects to a matched load, the output signal of PA can be expressed with a memoryless polynomial, as in the following equation:

$$\tilde{b}_{2-\text{match}}(n) = \sum_{k=1}^{K_1} \alpha_k \tilde{a}_1(n)|\tilde{a}_1(n)|^{k-1} \tag{11}$$

where α_k is the model coefficient. We can find that the TD-PHD model in (10) will also degrade to (11) without the excitation of $\tilde{a}_2(n)$, i.e., $\tilde{a}_2(n) = 0$. Therefore, (11) describes the nonlinear behavior of PA with the excitation of only an input signal $\tilde{a}_1(n)$.

As mentioned in Section II, the superposition principle is also applicable [36] such that the output signal can be regarded as the superposition of the nonlinear responses caused by $\tilde{a}_1(n)$ and $\tilde{a}_2(n)$. If the PA connects to a mismatched load with a load reflection coefficient of Γ, the nonlinear response generated by the excitation of $\tilde{a}_2(n)$ will be involved in (11), leading to the memoryless TD-PHD model in (10) with $M_1 = M_2 = M_3 = P_1 = P_2 = P_3 = 0$. The model coefficients in this case are denoted as α_k, β_k, and γ_k.

Since the nonlinear response is determined mainly by the input signal $\tilde{a}_1(n)$, while the reflection signal $\tilde{a}_2(n)$ will impose a small perturbation to the operation of the amplifier around the main operating point, we can assume that the PA's response induced only by the input signal $\tilde{a}_1(n)$, i.e., the first summations in (10), will barely be affected by the variation of the reflection signal $\tilde{a}_2(n)$. Then, when the PA's load coefficient changes to Γ_r while the average power, PAPR, and other characteristics of the original input signal $\tilde{a}_1(n)$ remain unchanged, the PA's output signal with load reflection coefficient Γ_r has the form as follows:

$$\tilde{b}_2^r(n) = \sum_{k=1}^{K_1} \alpha_k \tilde{a}_1(n)|\tilde{a}_1(n)|^{k-1} + \sum_{k=1}^{K_2} \beta_k^r \tilde{a}_2^r(n)|\tilde{a}_1(n)|^{k-1} + \sum_{k=1}^{K_3} \gamma_k^r \tilde{a}_1^2(n)\tilde{a}_2^{r*}(n)|\tilde{a}_1(n)|^{k-1} \tag{12}$$

where $\tilde{b}_2^r(n)$ and $\tilde{a}_2^r(n)$ denote the output signal and reflection signal of PA with load reflection coefficient Γ_r, respectively; and α_k, β_k^r, and γ_k^r denote the model coefficients. In this case, we can notice that the coefficients of basis functions $\tilde{a}_2^r(n)|\tilde{a}_1(n)|^{k-1}$ and $\tilde{a}_1^2(n)\tilde{a}_2^{r*}(n)|\tilde{a}_1(n)|^{k-1}$ change from β_k and γ_k to β_k^r and γ_k^r for the sake of load variation, while the coefficients α_k of functions $\tilde{a}_1(n)|\tilde{a}_1(n)|^{k-1}$ are supposed to be unchanged.

The load reflection coefficient Γ is defined in narrowband scenarios as follows:

$$\Gamma = \frac{\tilde{a}_2}{\tilde{b}_2}. \tag{13}$$

Then, the reflection signal $\tilde{a}_2(n)$ and $\tilde{a}_2^r(n)$ can be represented by the output signal $\tilde{b}_2(n)$ and $\tilde{b}_2^r(n)$, i.e., $\tilde{a}_2(n) = \Gamma \cdot \tilde{b}_2(n)$ and $\tilde{a}_2^r(n) = \Gamma_r \cdot \tilde{b}_2^r(n)$. Usually, the nonlinear components of the amplifier are much smaller than the linear components. Then, high-order terms in $\tilde{b}_2(n)$ and $\tilde{b}_2^r(n)$

can be ignored to represent $\tilde{a}_2(n)$ and $\tilde{a}_2^r(n)$, as in the following equation:

$$\tilde{a}_2(n) = \Gamma \cdot \tilde{b}_2(n) \approx \Gamma \cdot (\alpha_1 \tilde{a}_1(n) + \beta_1 \tilde{a}_2(n)) \quad (14)$$

$$\tilde{a}_2^r(n) = \Gamma_r \cdot \tilde{b}_2^r(n) \approx \Gamma_r \cdot \left(\alpha_1 \tilde{a}_1(n) + \beta_1^r \tilde{a}_2^r(n)\right). \quad (15)$$

$\tilde{a}_2(n)$ and $\tilde{a}_2^r(n)$ can be expressed in a concise form by recombining (14) and (15), as in the following equation:

$$\tilde{a}_2(n) = \frac{\Gamma}{1 - \Gamma \cdot \beta_1} \alpha_1 \tilde{a}_1(n) \quad (16)$$

$$\tilde{a}_2^r(n) = \frac{\Gamma_r}{1 - \Gamma_r \cdot \beta_1^r} \alpha_1 \tilde{a}_1(n). \quad (17)$$

Then, we can find the relationship between $\tilde{a}_2(n)$ and $\tilde{a}_2^r(n)$, as shown in the following:

$$\tilde{a}_2^r(n) = \frac{\Gamma_r}{\Gamma} \cdot \frac{1 - \Gamma \cdot \beta_1}{1 - \Gamma_r \cdot \beta_1^r} \cdot \tilde{a}_2(n). \quad (18)$$

Substituting (18) into (12), the output signal $\tilde{b}_2^r(n)$ with load condition Γ_r will be expressed by the original input signal $\tilde{a}_1(n)$ and the reflection signal $\tilde{a}_2(n)$ before load variation, as shown in the following:

$$\begin{aligned} \tilde{b}_2^r(n) = & \sum_{k=1}^{K_1} \alpha_k \tilde{a}_1(n) |\tilde{a}_1(n)|^{k-1} \\ & + \sum_{k=1}^{K_2} \beta_k' \cdot \frac{\Gamma_r}{\Gamma} \cdot \tilde{a}_2(n) |\tilde{a}_1(n)|^{k-1} \\ & + \sum_{k=1}^{K_3} \gamma_k' \cdot \left(\frac{\Gamma_r}{\Gamma}\right)^* \cdot \tilde{a}_2^*(n) \tilde{a}_1^2(n) |\tilde{a}_1(n)|^{k-1} \end{aligned} \quad (19)$$

where

$$\beta_k' = \beta_k^r \frac{1 - \Gamma \beta_1}{1 - \Gamma_r \beta_1^r}, \quad \gamma_k' = \gamma_k^r \left(\frac{1 - \Gamma \beta_1}{1 - \Gamma_r \beta_1^r}\right)^*. \quad (20)$$

In (19), α_k, $\beta_k' \cdot (\Gamma_r / \Gamma)$, and $\gamma_k' \cdot (\Gamma_r / \Gamma)^*$ form the new model coefficients. It can be seen that the output signals $\tilde{b}_2(n)$ and $\tilde{b}_2^r(n)$ are modeled with the same basis functions composed of the reflection signal $\tilde{a}_2(n)$ with load condition Γ and the original input signal $\tilde{a}_1(n)$. In such a case, if we can find a set of model coefficients $\tilde{\alpha}_k$, $\tilde{\beta}_k$, and $\tilde{\gamma}_k$ that satisfies the following equation:

$$\begin{cases} y_{\text{ref}}(n) \approx \tilde{b}_2(n) \\ y_r(n) \approx \tilde{b}_2^r(n) \end{cases} \quad (21)$$

where

$$\begin{aligned} y_{\text{ref}}(n) = & \sum_{k=1}^{K_1} \tilde{\alpha}_k \tilde{a}_1(n) |\tilde{a}_1(n)|^{k-1} + \sum_{k=1}^{K_2} \tilde{\beta}_k \tilde{a}_2(n) |\tilde{a}_1(n)|^{k-1} \\ & + \sum_{k=1}^{K_3} \tilde{\gamma}_k \tilde{a}_2^*(n) \tilde{a}_1^2(n) |\tilde{a}_1(n)|^{k-1} \end{aligned} \quad (22)$$

$$\begin{aligned} y_r(n) = & \sum_{k=1}^{K_1} \tilde{\alpha}_k \tilde{a}_1(n) |\tilde{a}_1(n)|^{k-1} + \sum_{k=1}^{K_2} \tilde{\beta}_k \cdot \frac{\Gamma_r}{\Gamma} \cdot \tilde{a}_2(n) |\tilde{a}_1(n)|^{k-1} \\ & + \sum_{k=1}^{K_3} \tilde{\gamma}_k \cdot \left(\frac{\Gamma_r}{\Gamma}\right)^* \cdot \tilde{a}_2^*(n) \tilde{a}_1^2(n) |\tilde{a}_1(n)|^{k-1}. \end{aligned} \quad (23)$$

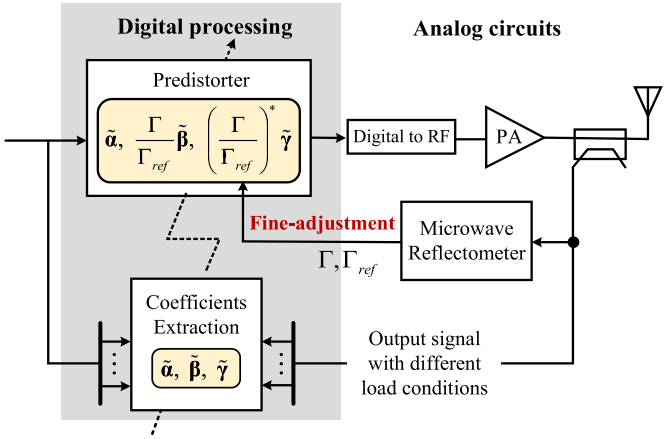

Fig. 4. Block diagram of the proposed LMT-DPD system.

Then, when the load reflection coefficient changes from Γ to Γ_r, the expressions of the PA's output signal with both load conditions have the same basis functions but the different model coefficients, which are modified from $(\tilde{\boldsymbol{\alpha}}, \tilde{\boldsymbol{\beta}}, \tilde{\boldsymbol{\gamma}})$ to $[\tilde{\boldsymbol{\alpha}}, (\Gamma_r / \Gamma)\tilde{\boldsymbol{\beta}}, (\Gamma_r / \Gamma)^* \tilde{\boldsymbol{\gamma}}]$. This favorable phenomenon indicates that, if such a set of appropriate model coefficients $(\tilde{\boldsymbol{\alpha}}, \tilde{\boldsymbol{\beta}}, \tilde{\boldsymbol{\gamma}})$ can be obtained, we only need to adjust the model coefficients according to the real-time load reflection coefficient when the PA's load conditions change, rather than recalibrating its coefficients through the adaptive identification algorithm. In this way, frequent calibrations of the model coefficients are avoided. At the same time, it enables fast adaption of the DPD system to track the variation of the PA's nonlinear behavior in mobile terminals.

Fig. 4 shows the structure of the proposed LMT-DPD technique. Compared to the typical DPD system, a microwave reflectometer is needed to provide the load reflection coefficient. Fortunately, adaptive antenna impedance matching techniques are widely employed in commercial mobile handsets for bringing the load impedance from the extreme scenarios where high VSWRs such as 8:1 or more are experienced to an acceptable level of VSWR within 3:1 [38]. A typical closed-loop antenna impedance tuning module comprises a reflectometer (RF sensor) to detect the impedance mismatch, an impedance tuner to stabilize the input impedance of the antenna, and a controller running the tuning algorithm based on the real-time measured impedance value from the RF sensor [39], [40]. Therefore, since the adaptive antenna impedance tuning module is necessary for commercial mobile handsets, the expected reflection coefficients in the proposed LMT-DPD method can be obtained from the involved reflectometers directly.

The update of the predistorter's model includes two major steps. The fixed coefficients $(\tilde{\boldsymbol{\alpha}}, \tilde{\boldsymbol{\beta}}, \tilde{\boldsymbol{\gamma}})$ are suitable within a wide load variation range, where the predistorter's coefficients will be modified as $[\tilde{\boldsymbol{\alpha}}, (\Gamma_r / \Gamma)\tilde{\boldsymbol{\beta}}, (\Gamma_r / \Gamma)^* \tilde{\boldsymbol{\gamma}}]$ according to the real-time load reflection coefficient when the variations of the load conditions occur. Then, if the working state of the amplifier changes significantly due to temperature, average power, load mismatch, and so on, the coefficients $(\tilde{\boldsymbol{\alpha}}, \tilde{\boldsymbol{\beta}}, \tilde{\boldsymbol{\gamma}})$ should be recalibrated with the LS algorithm.

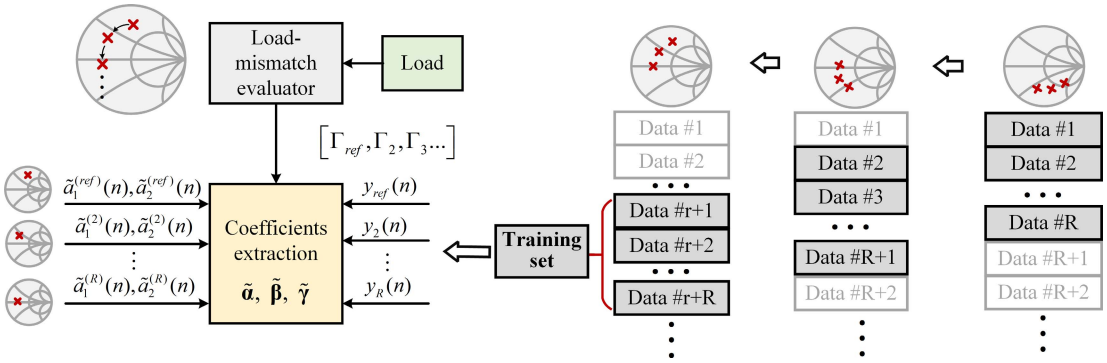

Fig. 5. Block diagram of the coefficients extraction module.

B. Coefficients Extraction Method

According to the above analysis, the LMT-DPD technique must obtain the appropriate fixed model coefficients $(\tilde{\boldsymbol{\alpha}}, \tilde{\boldsymbol{\beta}}, \tilde{\boldsymbol{\gamma}})$. In this section, the extraction method of the fixed coefficients will be introduced in detail. Note that the load match condition is excluded in the following derivations, i.e., the reflection coefficient is nonzero.

1) Calculation of the Reflection Signal $\tilde{a}_2(n)$: First, we will introduce the construction method for the reflection signal $\tilde{a}_2(n)$. Considering that the reflection coefficient is dynamic within a relatively wide signal bandwidth, $\tilde{a}_2(n)$ can be modeled as follows:

$$\tilde{a}_2(n) = \sum_{q=0}^{Q} \lambda_q \tilde{b}_2(n-q) \tag{24}$$

where λ_q is the coefficient. Then, we can simplify the expression of $\tilde{a}_2(n)$ by ignoring high-order terms in $\tilde{b}_2(n)$, resulting in the following:

$$\begin{aligned}\tilde{a}_2(n) &\approx \sum_{q=0}^{Q} \alpha_1 \lambda_q \tilde{a}_1(n-q) + \sum_{q=0}^{Q} \beta_1 \lambda_q \tilde{a}_2(n-q) \\ &= \sum_{q=0}^{Q} d_q \tilde{a}_1(n-q)\end{aligned} \tag{25}$$

where d_q denotes the recombined model coefficients. Note that this assumption to derive (25) has been used in prior literature [41], [42].

From (25), we can find that the calculation of $\tilde{a}_2(n)$ still requires Q complex multipliers since each d_q can be normalized with the first coefficient d_0. Moreover, the identification of coefficients d_q will also consume a certain amount of computation resources. Therefore, considering that the application scenarios of this DPD technique are mobile terminals with stringent complexity limitations, we might assume that the recombined coefficients d_q are equal to 1. Then, the estimated $\tilde{a}_2(n)$ has the form as follows:

$$\tilde{a}_{2\text{est}}(n) \approx \sum_{q=0}^{Q} \tilde{a}_1(n-q). \tag{26}$$

With (26), one can calculate the reflection signal $\tilde{a}_2(n)$ directly from the original input signal $\tilde{a}_1(n)$, rather than measuring $\tilde{a}_2(n)$ at the PA output in real time. It is worth noticing that although (26) is an approximate representation of $\tilde{a}_2(n)$, the effectiveness of the proposed LMT-DPD technique and TD-PHD model will not be influenced too much, as analyzed in the Appendix.

2) Extraction of the Fixed Model Coefficients: The coefficient extraction module is supposed to identify the fixed coefficients $(\tilde{\boldsymbol{\alpha}}, \tilde{\boldsymbol{\beta}}, \tilde{\boldsymbol{\gamma}})$ using multiple sets of PA input and output signals under different load-mismatch conditions to cover a sufficient load variation range. Fig. 5 presents the block diagram of the coefficient extraction module. Multiple sets of data are used to calibrate the coefficients $(\tilde{\boldsymbol{\alpha}}, \tilde{\boldsymbol{\beta}}, \tilde{\boldsymbol{\gamma}})$, including the input, output, and load reflection coefficients of PA under different load conditions. The reflectometer in the adaptive antenna impedance tuning module can provide the requirement of the load reflection coefficients $[\Gamma_1, \Gamma_2, \ldots, \Gamma_r, \ldots, \Gamma_R]$. Notably, each "Data #" block in Fig. 5 contains the PA's input and output information at the corresponding load condition.

Considering the memory effect, the output signal $y_{\text{ref}}(n)$ of PA with load coefficient Γ_{ref} is described with the TD-PHD model in (10). Equation (10) can be written in the matrix form as

$$\mathbf{y}_{\text{ref}} = \begin{bmatrix} \mathbf{A}_1^{\text{ref}} & \mathbf{A}_2^{\text{ref}} & \mathbf{A}_3^{\text{ref}} \end{bmatrix} \begin{bmatrix} \tilde{\boldsymbol{\alpha}} \\ \tilde{\boldsymbol{\beta}} \\ \tilde{\boldsymbol{\gamma}} \end{bmatrix} \tag{27}$$

where $\tilde{\boldsymbol{\alpha}} = [\tilde{\alpha}_{10}, \tilde{\alpha}_{11}, \ldots, \tilde{\alpha}_{K_1,M_1}]^T$, $\tilde{\boldsymbol{\beta}} = [\tilde{\beta}_0^1, \ldots, \tilde{\beta}_{P_1}^1, \tilde{\beta}_{200}^2, \ldots, \tilde{\beta}_{K_2,M_2,P_2}^2]^T$, and $\tilde{\boldsymbol{\gamma}} = [\tilde{\gamma}_{100}, \tilde{\gamma}_{101}, \ldots, \tilde{\gamma}_{K_3,M_3,P_3}]^T$ are the coefficients' vectors; $\mathbf{y}_{\text{ref}} = [y_{\text{ref}}(n), y_{\text{ref}}(n+1), \ldots, y_{\text{ref}}(n+N-1)]^T$ denotes the column vector composed of the output signal samples, with N the number of samples; and $\mathbf{A}_1^{\text{ref}}$, $\mathbf{A}_2^{\text{ref}}$, and $\mathbf{A}_3^{\text{ref}}$ are the basis function matrixes composed of the input signal $\tilde{a}_1^{(\text{ref})}(n)$ and reflection signals $\tilde{a}_2^{(\text{ref})}(n)$ of PA with load coefficient Γ_{ref}, as in (28)–(30), shown at the bottom of the next page, where

$$\begin{aligned}
f_{\text{km}}^1(i) &= \tilde{a}_1^{(\text{ref})}(n-m+i)\left|\tilde{a}_1^{(\text{ref})}(n-m+i)\right|^{k-1} \\
f_p^2(i) &= \tilde{a}_2^{(\text{ref})}(n-p+i) \\
f_{\text{kmp}}^3(i) &= \tilde{a}_2^{(\text{ref})}(n-p+i)\left|\tilde{a}_1^{(\text{ref})}(n-m+i)\right|^{k-1} \\
f_{\text{kmp}}^4(i) &= \left(\tilde{a}_2^{(\text{ref})}(n-p+i)\right)^*\left(\tilde{a}_1^{(\text{ref})}(n-m+i)\right)^2 \\
&\quad \times\left|\tilde{a}_1^{(\text{ref})}(n-m+i)\right|^{k-1}.
\end{aligned}$$

When the PA's load reflection coefficient changes to Γ_r, the corresponding input and output signal samples are denoted as $\tilde{a}_1^{(r)}(n)$ and $y_r(n)$, respectively, where $\tilde{a}_1^{(r)}(n)$ and $\tilde{a}_1^{(\text{ref})}(n)$ are supposed to have similar characteristics such as average power and PAPR. According to (23), the PA's output signal samples can be estimated in the matrix form as follows:

$$\mathbf{y}_r = \begin{bmatrix} \mathbf{A}_1^r & \mathbf{A}_2^r & \mathbf{A}_3^r \end{bmatrix} \begin{bmatrix} \tilde{\boldsymbol{\alpha}} \\ \Gamma_r/\Gamma_{\text{ref}} \cdot \tilde{\boldsymbol{\beta}} \\ \Gamma_r^*/\Gamma_{\text{ref}}^* \cdot \tilde{\boldsymbol{\gamma}} \end{bmatrix}. \tag{31}$$

Then, (31) can now be rewritten by embedding the adjustment factors $\Gamma_r/\Gamma_{\text{ref}}$ and $(\Gamma_r/\Gamma_{\text{ref}})^*$ into the basis function matrixes, as in the following equation:

$$\mathbf{y}_r = \begin{bmatrix} \mathbf{A}_1^r & \dfrac{\Gamma_r}{\Gamma_{\text{ref}}}\mathbf{A}_2^r & \dfrac{\Gamma_r^*}{\Gamma_{\text{ref}}^*}\mathbf{A}_3^r \end{bmatrix} \begin{bmatrix} \tilde{\boldsymbol{\alpha}} \\ \tilde{\boldsymbol{\beta}} \\ \tilde{\boldsymbol{\gamma}} \end{bmatrix}. \tag{32}$$

Finally, if the input and the output information of PA with load conditions of $[\Gamma_{\text{ref}}, \Gamma_2, \ldots, \Gamma_r, \ldots, \Gamma_R]$ are sampled, the simultaneous equations describing all output signals will be given by

$$\begin{bmatrix} \mathbf{y}_{\text{ref}} \\ \mathbf{y}_2 \\ \vdots \\ \mathbf{y}_R \end{bmatrix} = \begin{bmatrix} \mathbf{A}_1^{\text{ref}} & \mathbf{A}_2^{\text{ref}} & \mathbf{A}_3^{\text{ref}} \\ \mathbf{A}_1^2 & \Gamma_2/\Gamma_{\text{ref}}\mathbf{A}_2^2 & \Gamma_1^*/\Gamma_{\text{ref}}^*\mathbf{A}_3^2 \\ \vdots & \vdots & \vdots \\ \mathbf{A}_1^R & \Gamma_R/\Gamma_{\text{ref}}\mathbf{A}_2^R & \Gamma_R^*/\Gamma_{\text{ref}}^*\mathbf{A}_3^R \end{bmatrix} \begin{bmatrix} \tilde{\boldsymbol{\alpha}} \\ \tilde{\boldsymbol{\beta}} \\ \tilde{\boldsymbol{\gamma}} \end{bmatrix}. \tag{33}$$

Then, the fixed coefficients $\tilde{\boldsymbol{\alpha}}, \tilde{\boldsymbol{\beta}}$, and $\tilde{\boldsymbol{\gamma}}$ can be estimated using the LS solver, as in the following equation:

$$\mathbf{v} = \left(\mathbf{X}^H\mathbf{X}\right)^{-1}\mathbf{X}^H\mathbf{Y} \tag{34}$$

where

$$\mathbf{v} = \begin{bmatrix} \tilde{\boldsymbol{\alpha}} \\ \tilde{\boldsymbol{\beta}} \\ \tilde{\boldsymbol{\gamma}} \end{bmatrix}, \quad \mathbf{X} = \begin{bmatrix} \mathbf{A}_1^{\text{ref}} & \mathbf{A}_2^{\text{ref}} & \mathbf{A}_3^{\text{ref}} \\ \mathbf{A}_1^2 & \Gamma_2/\Gamma_{\text{ref}}\mathbf{A}_2^2 & \Gamma_2^*/\Gamma_{\text{ref}}^*\mathbf{A}_3^2 \\ \vdots & \vdots & \vdots \\ \mathbf{A}_1^R & \Gamma_R/\Gamma_{\text{ref}}\mathbf{A}_2^R & \Gamma_R^*/\Gamma_{\text{ref}}^*\mathbf{A}_3^R \end{bmatrix}$$

$$\mathbf{Y} = \begin{bmatrix} \mathbf{y}_{\text{ref}} \\ \mathbf{y}_2 \\ \vdots \\ \mathbf{y}_R \end{bmatrix}.$$

It is worth noting that the fixed coefficients of the predistorter can be identified by swapping the input and output in (34). Then, when the PA's load reflection coefficients vary within the identification load range, the real-time predistorter's coefficients are obtained by embedding the corresponding adjustment factors into the fixed coefficients, as already introduced in Section III-A. In addition, the fixed coefficients will be recalibrated if the load conditions of the PA change widely beyond $[\Gamma_{\text{ref}}, \Gamma_2, \ldots, \Gamma_r, \ldots, \Gamma_R]$.

C. Discussion on Complexity

In mobile handsets, the load impedance of PA often changes quickly as the equipment moves around. Since recalibrating the coefficients is time-consuming, the conventional DPD technique will extract and save multiple sets of coefficients for different load conditions to achieve a fast update of the predistorter's coefficients. The first advantage of the proposed technique is that it occupies less storage space in the terminals to save the coefficients since only a few sets of fixed coefficients are required in the proposed LMT-DPD, while the conventional DPD needs to save much more sets of coefficients corresponding to different load conditions. However, to extract the appropriate fixed model coefficients ($\tilde{\boldsymbol{\alpha}}, \tilde{\boldsymbol{\beta}}$, and $\tilde{\boldsymbol{\gamma}}$), the LMT-DPD technique needs multiple sets of PA's input and output signals under different load-mismatch conditions, which may lead to an increase in computation resources. Therefore, the complexity of identifying the fixed model coefficients is evaluated in terms of real-number multiplication and addition. Table I summarizes the times of real-number addition and multiplication of each operation required in the identification procedure [43]. Assuming that H_1, H_2, and H_3 denote the number of columns of the matrices $\mathbf{A}_1^r$, $\mathbf{A}_2^r$, and $\mathbf{A}_3^r$, respectively, then H denotes the total number of columns of the processed matrix, i.e., $H = H_1 + H_2 + H_3$.

$$\mathbf{A}_1 = \begin{bmatrix} f_{10}^1(0) & f_{11}^1(0) & \cdots & f_{K_1,M_1}^1(0) \\ f_{10}^1(1) & f_{11}^1(1) & \cdots & f_{K_1,M_1}^1(1) \\ \vdots & \vdots & \ddots & \vdots \\ f_{10}^1(N-1) & f_{11}^1(N-1) & \cdots & f_{K_1,M_1}^1(N-1) \end{bmatrix} \tag{28}$$

$$\mathbf{A}_2 = \begin{bmatrix} f_0^2(0) & \cdots & f_{P_1}^2(0) & f_{200}^3(0) & \cdots & f_{K_2,M_2,P_2}^3(0) \\ f_0^2(1) & \cdots & f_{P_1}^2(0) & f_{200}^3(1) & \cdots & f_{K_2,M_2,P_2}^3(1) \\ \vdots & \ddots & \vdots & \vdots & \ddots & \vdots \\ f_0^2(N-1) & \cdots & f_{P_1}^2(N-1) & f_{200}^3(N-1) & \cdots & f_{K_2,M_2,P_2}^3(N-1) \end{bmatrix} \tag{29}$$

$$\mathbf{A}_3 = \begin{bmatrix} f_{100}^4(0) & f_{101}^4(0) & \cdots & f_{K_3,M_3,P_3}^4(0) \\ f_{100}^4(1) & f_{101}^4(1) & \cdots & f_{K_3,M_3,P_3}^4(1) \\ \vdots & \vdots & \ddots & \vdots \\ f_{100}^4(N-1) & f_{101}^4(N-1) & \cdots & f_{K_3,M_3,P_3}^4(N-1) \end{bmatrix} \tag{30}$$

TABLE I
REAL-NUMBER ADDITIONS AND MULTIPLICATIONS OF EACH OPERATION

Operations	Additions	Multiplications
$\mathbf{A}$	0	$2HN$
$\mathbf{A}^H\mathbf{A}$	H^2N	$2H^2N$
$(\mathbf{A}^H\mathbf{A})^{-1}$	H^3	H^3
$\mathbf{A}^H\mathbf{x}$	$2HN$	$2HN$
$(\mathbf{A}^H\mathbf{A})^{-1}(\mathbf{A}^H\mathbf{x})$	$4H^2$	$4H^2$

According to (33) and (34), the size of the processed basis function matrix $\mathbf{X}$ for the LMT-DPD is $RN \times H$. On the other hand, the processed matrix for the conventional DPD has the size of $N \times H$. Assuming that the identification procedure will repeat R_1 times to extract the dedicated set of coefficients for different load-mismatch conditions, the total quantities of the conventional DPD with adaption and the proposed LMT-DPD, represented by the times of real-number multiplication and addition, are shown as follows:

$$O^{+}_{\text{conv.DPD}} = R_1\left(2NH + H^3 + NH^2 + 4H^2\right) \quad (35)$$

$$O^{\times}_{\text{conv.DPD}} = R_1\left(2NH^2 + 4NH + H^3 + 4H^2\right) \quad (36)$$

$$O^{+}_{\text{LMT-DPD}} = 2RNH + H^3 + RNH^2 + 4H^2 + 2N(R-1)(H - H_1) \quad (37)$$

$$O^{\times}_{\text{LMT-DPD}} = 2RNH^2 + 4RNH + H^3 + 4H^2 + 4N(R-1)(H - H_1) \quad (38)$$

where O^{+} and $O^{\times}$ represent the computational quantities of addition and multiplication, respectively. Usually, the sample length N is far larger than H, leading to the ratio between the proposed LMT-DPD and the conventional adaptive DPD as

$$\lim_{N\to\infty} \frac{O^{+}_{\text{LMT-DPD}}}{O^{+}_{\text{conv.DPD}}} < \frac{R}{R_1} \times \frac{H+4}{H+2} \quad (39)$$

$$\lim_{N\to\infty} \frac{O^{\times}_{\text{LMT-DPD}}}{O^{\times}_{\text{conv.DPD}}} < \frac{R}{R_1} \times \frac{H+4}{H+2}. \quad (40)$$

Equations (39) and (40) can roughly reveal the increase or decrease in computation resources of the proposed LMT-DPD method against conventional DPD. If the ratio R to R_1 exceeds 1, the proposed technique will consume more computational resources and vice versa. By carefully selecting the training sets to identify the fixed coefficients, the computational complexity of the LMT-DPD can be comparable to or even less than the conventional DPD method.

IV. MEASUREMENTS RESULTS

A. Experimental Setups

An experimental platform is set up to validate the performance of the proposed DPD technique, as shown in Fig. 6. The measurements are applied on the PA in a Skyworks sky58255-11 front-end module (FEM), operating at the center frequency of 4.6 GHz. The input signal is a 100-MHz bandwidth 5G NR signal with 256-QAM modulation and a 14-dB PAPR. The sampling rate of the input signal is 491.52 Msps. A vector signal transceiver (TRx) NI PxLe-5840 will generate the RF signal from baseband samples. An MPT-1807 tuner is inserted between the FEM and the antenna to control the load impedance of the amplifier. The coupler collects the feedback signals, which are then converted to baseband samples and uploaded to the personal computer (PC) by the TRx. All measured signals and DPD programs are processed in the PC running MATLAB.

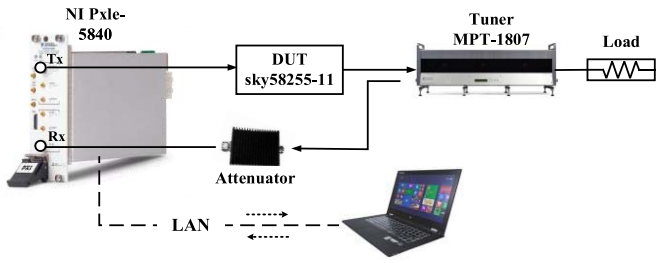

Fig. 6. Block diagram of the test bench.

B. Validation on the TD-PHD Model

First, we will introduce the experimental results of the TD-PHD model to demonstrate its superiority in the behavioral modeling and linearization of PA with load mismatch. The measurements are also carried out using a conventional GMP model for comparison, as in the following equation [44]:

$$\begin{aligned}\tilde{b}_2(n) = &\sum_{k=1}^{K}\sum_{m=0}^{M} w^1_{\text{km}}\tilde{a}_1(n-m)|\tilde{a}_1(n-m)|^{k-1} \\ &+ \sum_{k=2}^{K}\sum_{m=0}^{M}\sum_{p=1}^{P} w^2_{\text{kmp}}\tilde{a}_1(n-m)|\tilde{a}_1(n-m-p)|^{k-1} \\ &+ \sum_{k=2}^{K}\sum_{m=0}^{M}\sum_{p=1}^{P} w^3_{\text{kmp}}\tilde{a}_1(n-m)|\tilde{a}_1(n-m+p)|^{k-1}\end{aligned} \quad (41)$$

where w^1_{km}, w^2_{kmp}, and w^3_{kmp} are the model coefficients. In the measurement, the parameters of the GMP model are set as $K = 7$, $P = 2$, and $M = 3$, leading to total 124 coefficients. The TD-PHD in (10) has total 123 coefficients with $Q = 4$, $K_1 = K_2 = 7$, $K_3 = 5$, $M_1 = M_2 = M_3 = 2$, and $P_2 = P_3 = 2$.

The modeling accuracy of the TD-PHD model and GMP model is evaluated in the forward modeling process by sweeping the load conditions of the PA. In this evaluation, the coefficients of TD-PHD model and GMP model are reextracted for each load condition. Fig. 7 presents the measured normalized mean square errors (NMSEs) of the PA's original input and output signal under different load conditions and the forward modeling NMSEs achieved by the TD-PHD and GMP models. The NMSE values between the original input and output signal are from –27 to –17 dB. The nonlinear characteristics of the PA change obviously according to the load conditions, revealing that the PA's nonlinear behaviors are very sensitive to its load conditions. As it can be seen, the modeling accuracy of the GMP model is only –34 dB, while the TD-PHD model realizes approaching –37-dB NMSE performance among a wide load impedance range. By introducing the phase differences

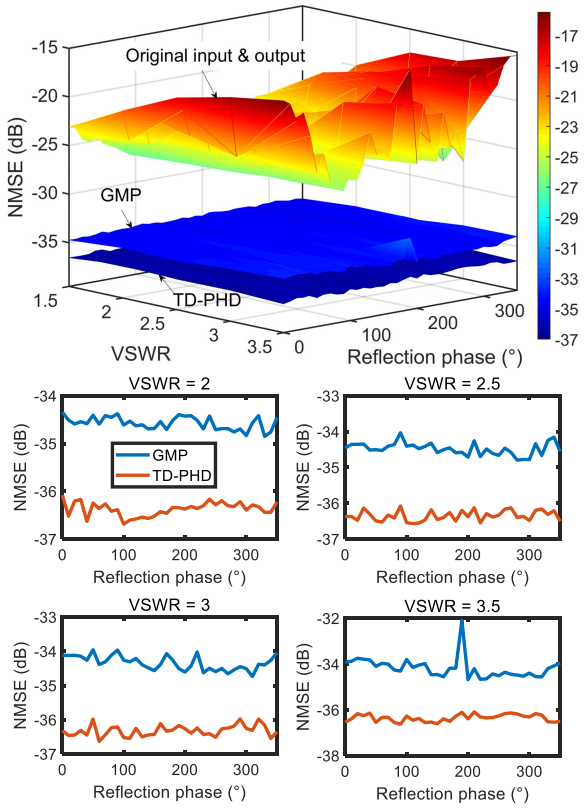

Fig. 7. Forward modeling NMSEs of the TD-PHD and GMP models with different load conditions.

between the input and reflection signal, the TD-PHD model can characterize the nonlinear distortion of a load-mismatch PA more accurately than the conventional DPD models, such as GMP.

Furthermore, the TD-PHD and GMP models are also used for DPD linearization. Fig. 8 shows the PSDs of the PA's outputs with different load conditions. When connecting a mismatched load, the PA will demonstrate "unusual" nonlinear characteristics such as in-band spectral tilting and severe asymmetry out-of-band spectral regrowth. In such cases, the TD-PHD model achieves much better and more stable linearization performance than the conventional GMP model; it can significantly improve the modeling accuracy under load-mismatch scenarios.

C. Validations on the LMT-DPD Technique

The performance of the proposed LMT-DPD technique is validated based on the test bench shown in Fig. 6, along with the reference DPD, single-point (SP), and multipoint (MTP) coefficient extraction strategies for comparison. The reference DPD represents the ideal case where the DPD coefficients are reextracted at the same load condition as the validation. In the SP-DPD method, the predistorter's coefficients are extracted with the input and output data of PA under a reference load condition, while in the MTP-DPD, the coefficients are extracted with multiple input and output signals of PA under different load conditions. Accordingly, the coefficients

TABLE II
TRAINING SETS OF SP-DPD, MTP-DPD, AND LMT-DPD TECHNIQUES

Training sets	LMT-DPD & MTP-DPD	SP-DPD
①	VSWR = 2, phase = [80° 100° 120° 140°]	VSWR = 2, phase = 100°
②	VSWR = 3, phase = [20° 40° 60°]	VSWR = 3, phase = 40°
③	VSWR = [1.7 2.0 2.3], phase = 90°	VSWR = 2, phase = 90°

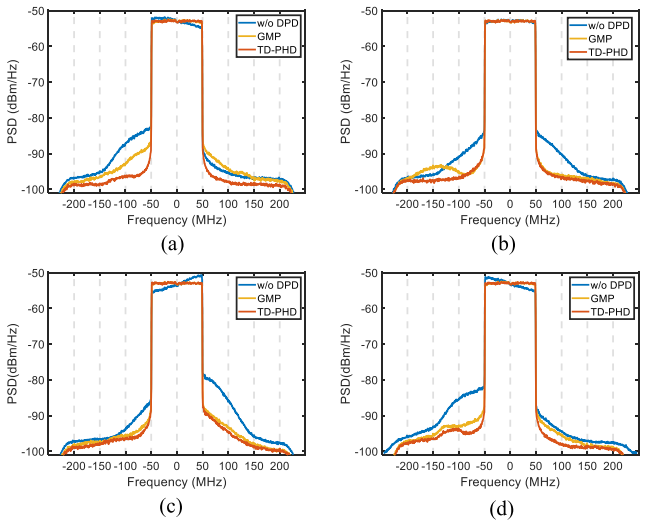

Fig. 8. Spectral plots of the PA's output with and without DPDs under different load conditions of (a) VSWR = 2.5 and reflection phase = 10°, (b) VSWR = 2.5 and reflection phase = 90°, (c) VSWR = 3.5 and reflection phase = 190°, and (d) VSWR = 3.5 and reflection phase = 290°.

in SP-DPD and MTP-DPD can be extracted as follows:

$$\mathbf{v}_{\mathrm{SP-DPD}} = \begin{bmatrix} \mathbf{A}_1^{\mathrm{ref}} & \mathbf{A}_2^{\mathrm{ref}} & \mathbf{A}_3^{\mathrm{ref}} \end{bmatrix}^{\dagger} \mathbf{y}_{\mathrm{ref}} \tag{42}$$

$$\mathbf{v}_{\mathrm{MTP-DPD}} = \begin{bmatrix} \mathbf{A}_1^{\mathrm{ref}} & \mathbf{A}_2^{\mathrm{ref}} & \mathbf{A}_3^{\mathrm{ref}} \\ \mathbf{A}_1^{2} & \mathbf{A}_2^{2} & \mathbf{A}_3^{2} \\ \vdots & \vdots & \vdots \\ \mathbf{A}_1^{R} & \mathbf{A}_2^{R} & \mathbf{A}_3^{R} \end{bmatrix}^{\dagger} \begin{bmatrix} \mathbf{y}_{\mathrm{ref}} \\ \mathbf{y}_2 \\ \vdots \\ \mathbf{y}_R \end{bmatrix} \tag{43}$$

where $\mathbf{A}^{\dagger}$ is the Moore–Penrose pseudoinverse given by $\mathbf{A}^{\dagger} = \left(\mathbf{A}^H\mathbf{A}\right)^{-1}\mathbf{A}^H$. Then, we reuse the coefficients $\mathbf{v}_{\mathrm{SP-DPD}}$ and $\mathbf{v}_{\mathrm{MTP-DPD}}$ of SP-DPD and MTP-DPD for the linearization of PA during load impedance variations.

The experimental validations are carried out among a relatively wide load impedance range. Table II summarizes the training sets of SP-DPD, MTP-DPD, and the proposed LMT-DPD technique. Since both the MTP-DPD and LMT-DPD need multiple PA's input and output signals under different load conditions to identify the coefficients, they share the same training sets for a fair comparison.

The NMSE, error vector magnitude (EVM), adjacent channel power ratios (ACPRs), and power spectral densities (PSDs) of different DPD schemes under various load conditions are observed for evaluations of linearity. The linearization results of the above DPD techniques with training sets ①, ②, and ③

TABLE III
LINEARIZATION RESULTS OF DIFFERENT DPD TECHNIQUES WITH TRAINING SET ①

Load conditions	Metrics	w/o DPD	Ref. DPD	SP-DPD	MTP-DPD	LMT-DPD
VSWR = 2 Reflection phase = 70°	ACPR	-36.2/-38.8 dBc	-46.3/-46.0 dBc	-42.6/-41.7 dBc	-43.1/-41.4 dBc	-44.9/-45.1 dBc
	NMSE	-25.12 dB	-34.11 dB	-27.85 dB	-27.49 dB	-32.14 dB
	EVM	2.73 %	0.74 %	1.10 %	1.20 %	0.84 %
VSWR = 2 Reflection phase = 90°	ACPR	-37.0/-36.6 dBc	-45.7/-45.4 dBc	-45.0/-44.5 dBc	-44.4/-43.4 dBc	-45.8/-45.3 dBc
	NMSE	-26.72 dB	-33.46 dB	-32.37 dB	-31.82 dB	-33.06 dB
	EVM	3.04 %	0.78 %	0.84 %	0.97 %	0.77 %
VSWR = 2 Reflection phase = 110°	ACPR	-37.5/-34.6 dBc	-45.2/-45.0 dBc	-44.5/-44.9 dBc	-44.7/-44.4 dBc	-45.4/-44.7 dBc
	NMSE	-26.80 dB	-33.31 dB	-32.82 dB	-33.15 dB	-33.55 dB
	EVM	3.35 %	0.82 %	0.81 %	0.86 %	0.79 %
VSWR = 2 Reflection phase = 130°	ACPR	-37.2/-33.5 dBc	-45.3/-45.0 dBc	-43.6/-43.0 dBc	-43.5/-43.5 dBc	-45.4/-44.6 dBc
	NMSE	-26.21 dB	-33.09 dB	-31.27 dB	-31.66 dB	-33.00 dB
	EVM	3.57 %	0.79 %	0.98 %	0.98 %	0.80 %
VSWR = 2 Reflection phase = 150°	ACPR	-36.7/-33.1 dBc	-45.0/-45.0 dBc	-41.2/-41.2 dBc	-42.4/-42.6 dBc	-44.6/-44.0 dBc
	NMSE	-25.84 dB	-33.38 dB	-30.08 dB	-30.84 dB	-32.41 dB
	EVM	3.66 %	0.83 %	1.16 %	1.12 %	0.95 %
VSWR = 2 Reflection phase = 160°	ACPR	-36.7/-32.7 dBc	-44.3/-44.7 dBc	-40.3/-39.8 dBc	-41.5/-42.0 dBc	-43.4/-43.2 dBc
	NMSE	-25.27 dB	-32.92 dB	-28.36 dB	-29.09 dB	-31.73 dB
	EVM	3.69 %	0.91 %	1.28 %	1.22 %	1.07 %

TABLE IV
LINEARIZATION RESULTS OF DIFFERENT DPD TECHNIQUES WITH TRAINING SET ②

Load conditions	Metrics	w/o DPD	Ref. DPD	SP-DPD	MTP-DPD	LMT-DPD
VSWR = 3 Reflection phase = 10°	ACPR	-35.6/-42.2 dBc	-45.8/-44.7 dBc	-44.2/-42.1 dBc	-43.4/-41.4 dBc	-46.4/-44.0 dBc
	NMSE	-22.70 dB	-32.96 dB	-30.82 dB	-30.68 dB	-31.68 dB
	EVM	2.24 %	0.81 %	1.45 %	1.28 %	0.94 %
VSWR = 3 Reflection phase = 30°	ACPR	-35.2/-41.2 dBc	-45.0/-43.6 dBc	-45.2/-44.3 dBc	-43.8/-42.7 dBc	-45.7/-44.3 dBc
	NMSE	-21.91 dB	-32.23 dB	-31.91 dB	-30.98 dB	-31.93 dB
	EVM	2.27 %	0.85 %	0.97 %	0.92 %	0.86 %
VSWR = 3 Reflection phase = 50°	ACPR	-35.5/-40.2 dBc	-45.4/-44.1 dBc	-45.0/-44.5 dBc	-43.7/-43.0 dBc	-45.5/-44.6 dBc
	NMSE	-23.26 dB	-32.55 dB	-31.63 dB	-31.72 dB	-32.36 dB
	EVM	2.37 %	0.79 %	0.94 %	0.97 %	0.84 %
VSWR = 3 Reflection phase = 70°	ACPR	-35.6/-39.3 dBc	-45.3/-44.7 dBc	-41.3/-41.7 dBc	-40.9/-41.5 dBc	-44.5/-44.3 dBc
	NMSE	-23.59 dB	-32.32 dB	-28.55 dB	-28.93 dB	-30.41 dB
	EVM	2.77 %	0.82 %	1.58 %	1.58 %	0.97 %
VSWR = 3 Reflection phase = 80°	ACPR	-36.5/-37.6 dBc	-45.4/-45.2 dBc	-39.9/-39.2 dBc	-39.8/-39.3 dBc	-43.2/-42.2 dBc
	NMSE	-25.41 dB	-32.82 dB	-25.72 dB	-26.39 dB	-30.21 dB
	EVM	3.03 %	0.79 %	1.94 %	1.93 %	1.17 %

are shown in Figs. 9–11, respectively, and training sets ① and ② in Tables III and IV, respectively. These results show that the SP-DPD and MTP-DPD disperse quickly as the load impedance varies, indicating that the DPD coefficients should be updated more frequently to achieve satisfying accuracy. The reference DPD technique achieves the best linearization

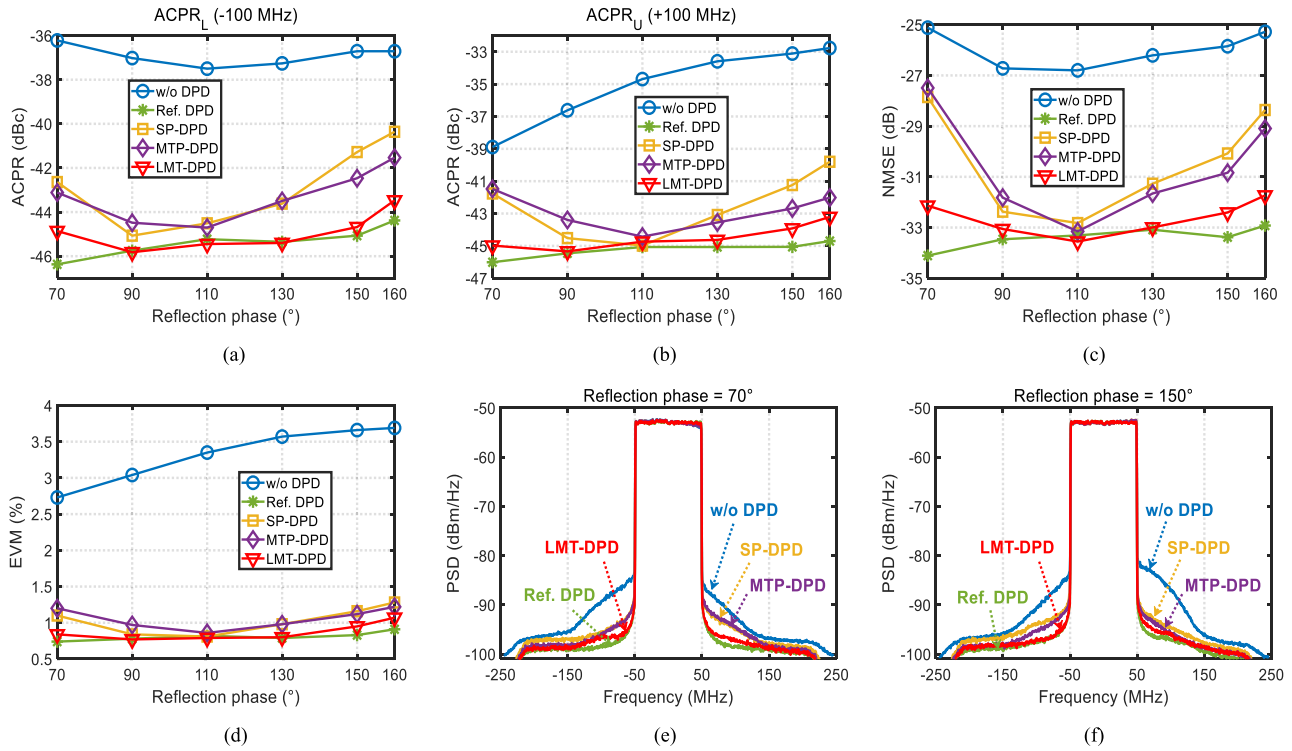

Fig. 9. Linearization results of different DPD techniques with training set ①: (a) lower band ACPR (–100 MHz), (b) upper band ACPR (+100 MHz), (c) NMSE, (d) EVM, (e) spectral plots of PA's output with reflection phase = 70° and VSWR = 2, and (f) spectral plots of PA's output with reflection phase = 150° and VSWR = 2.

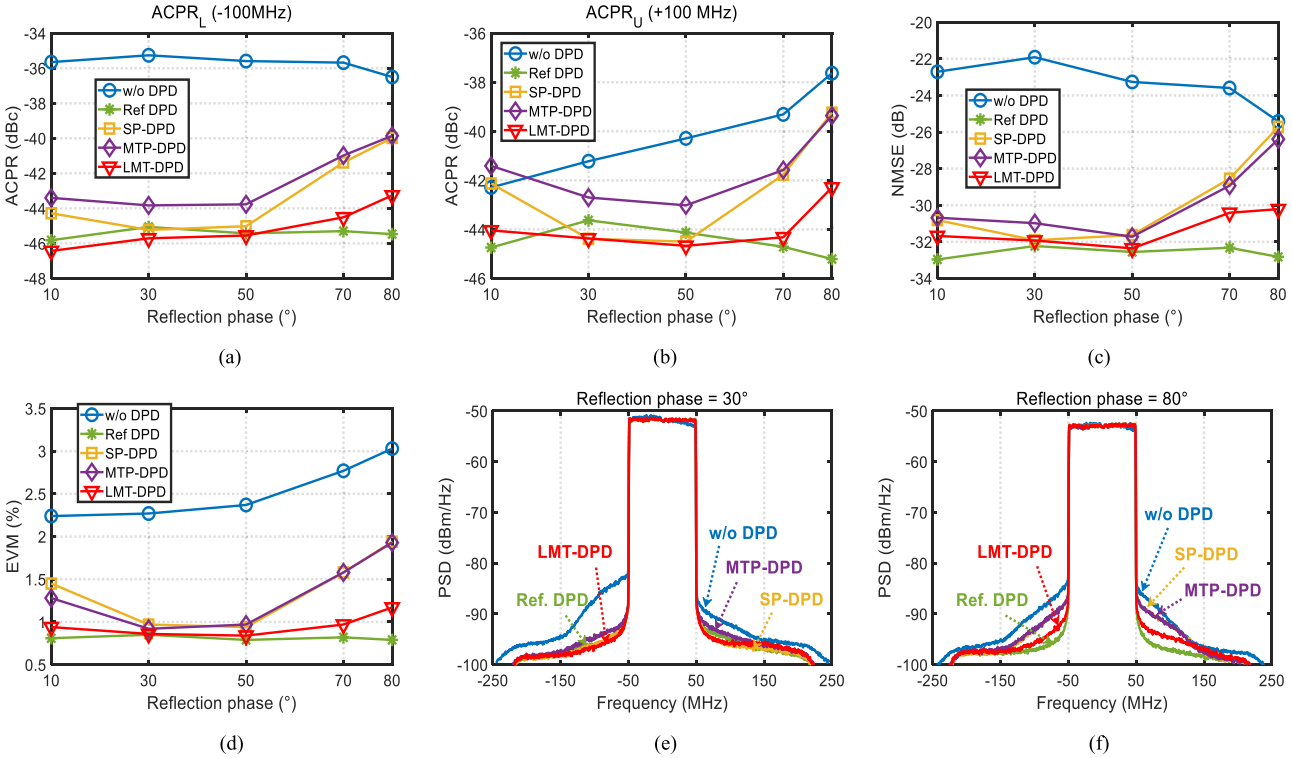

Fig. 10. Linearization results of different DPD techniques with training set ②: (a) lower band ACPR (–100 MHz), (b) upper band ACPR (+100 MHz), (c) NMSE, (d) EVM, (e) spectral plots of PA's output with reflection phase = 30° and VSWR = 3, and (f) spectral plots of PA's output with reflection phase = 80° and VSWR = 3.

performance in most load-mismatch conditions. However, it does need to recalibrate the predistorter's coefficients every time the VSWR or reflection phase changes. On the contrary, by embedding the load reflection coefficients and simply adjusting the model coefficients, the proposed LMT-DPD provides a suboptimal linearization performance comparable with the reference DPD and outperforms the SP-DPD and MTP-DPD obviously.

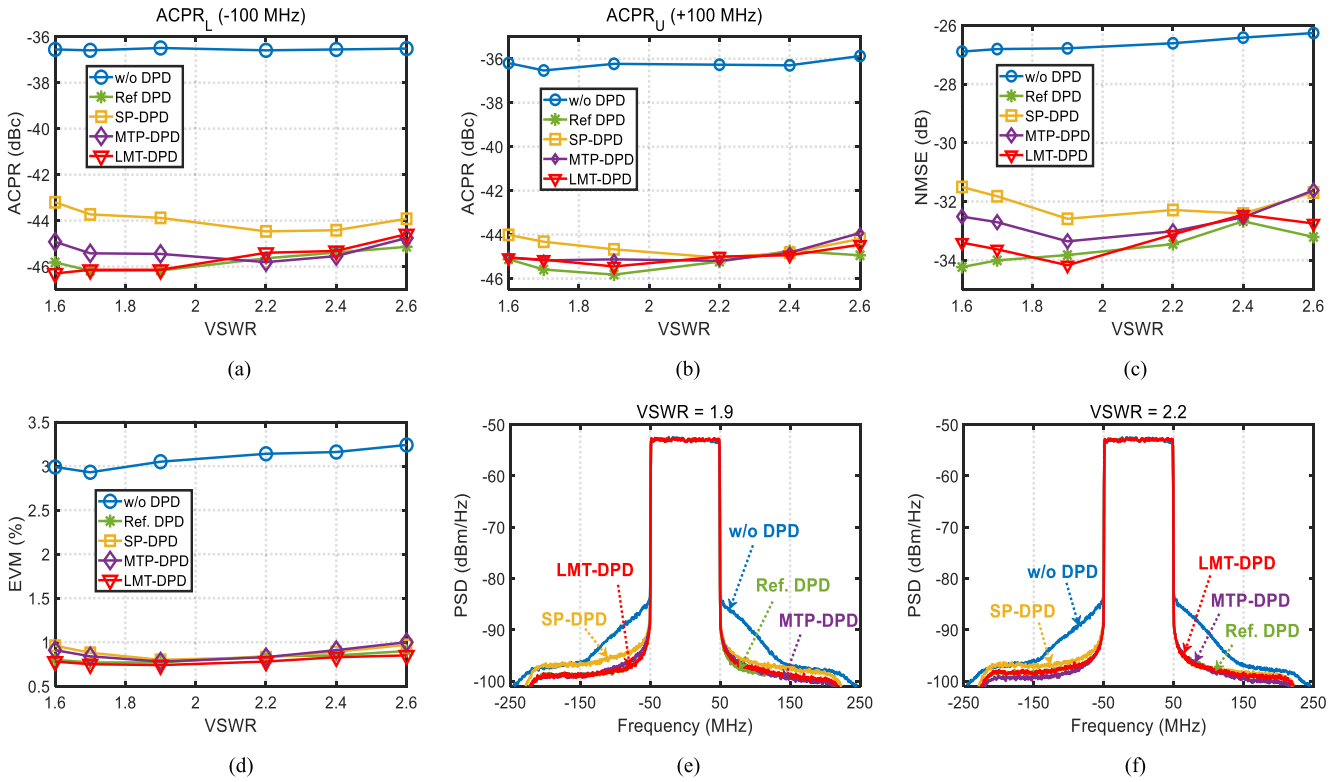

Fig. 11. Linearization results of different DPD techniques with training set ③: (a) lower band ACPR (–100 MHz), (b) upper band ACPR (+100 MHz), (c) NMSE, (d) EVM, (e) spectral plots of PA's output with reflection phase = 90° and VSWR = 1.9, and (f) spectral plots of PA's output with reflection phase = 90° and VSWR = 2.2.

Furthermore, the proposed LMT-DPD technique will be effective among a wide range of load impedances. For example, with training set ①, the linearization performance of the LMT-DPD is satisfying when the load reflection phase varies from 70° to 160°, giving the ACPR, NMSE, and EVM results of below –43 dBc, –31 dB, and 1.3%, respectively. In the second and third tests based on training sets ② and ③, similar results are obtained where the proposed LMT-DPD shows more stable linearization ability for different load-mismatch conditions than the SP-DPD and MTP-DPD techniques.

Among the above coefficient extraction techniques, the SP-DPD has the lowest identification complexity, yet its linearization performance is also poorer than the other methods. The MTP-DPD and LMT-DPD demonstrate comparable identification complexity for the model coefficients since they share the same training sets. However, the linearization performance of the LMT-DPD is better than the MTP-DPD. Furthermore, compared to the reference DPD, the LMT-DPD technique enables a faster update of its coefficients to track the variation of the PA's nonlinearity without losing much linearization accuracy. Based on the above experimental results, we can conclude that the proposed LMT-DPD technique is highly suitable for linearizing mobile-terminal PAs due to its faster update frequency, reduced complexity, and superior linearization performance.

V. Conclusion

The PA will suffer from severe nonlinear distortions in wireless mobile terminals due to the load-mismatch phenomenon. Linearization of a terminal PA involves unique challenges. Specifically, the DPD technique is supposed to track the nonlinearity variation of PA operating in complicated environments. To resolve this issue, a load-mismatch tracking DPD technique is proposed in this article to linearize mobile-terminal PAs. First, the TD-PHD model is introduced to compensate for the nonlinear distortions of PA under load-mismatch conditions. Based on the superposition principle and the TD-PHD model, the LMT-DPD technique is derived. By embedding the real-time load reflection coefficient in the fixed coefficients, the LMT-DPD enables fast and automatic adjustment of the predistorter's coefficients to adapt to the PA's nonlinearities without recalibration. Measurement results on a mobile-terminal PA at 4.6 GHz with 100-MHz bandwidth 5G NR signal are presented to benchmark the proposed DPD technique against the existing coefficients update strategies. The experimental results indicate that the proposed LMT-DPD technique can achieve excellent linearization performance for mobile-terminal PAs with varying load impedances.

Appendix

Considering that each coefficient d_q in (25) can be normalized with d_0, the reflection signal $\tilde{a}_2(n)$ can be expressed as

$$\begin{aligned}\tilde{a}_2(n) &\approx \tilde{a}_1(n) + \sum_{q=1}^{Q} d_q/d_0 \tilde{a}_1(n-q) \\ &= \tilde{a}_{2\text{est}}(n) + \varepsilon(n) \end{aligned} \tag{44}$$

where $\tilde{a}_{2\text{est}}(n)$ denotes the estimated signal obtained by (26) and $\varepsilon(n) = \sum_{q=1}^{Q} \left(d_q/d_0 - 1\right)\tilde{a}_1(n-q)$ denotes the construction error signal.

Substituting (44) into (10) and recombining the basis functions, the actual output signal $\tilde{b}_2(n)$ is expressed by the TD-PHD model as

$$\begin{aligned}\tilde{b}_2(n) = &\sum_{k=1}^{K_1}\sum_{m=0}^{M_1}\alpha_{\mathrm{km}}\tilde{a}_1(n-m)|\tilde{a}_1(n-m)|^{k-1}\\ &+\sum_{p=0}^{P_1}\beta_p^1\tilde{a}_{2\mathrm{est}}(n-p)\\ &+\sum_{k=2}^{K_2}\sum_{m=0}^{M_2}\sum_{p=0}^{P_2}\beta_{\mathrm{kmp}}^2\tilde{a}_{2\mathrm{est}}(n-p)|\tilde{a}_1(n-m)|^{k-1}\\ &+\sum_{k=1}^{K_3}\sum_{m=0}^{M_3}\sum_{p=0}^{P_3}\gamma_{\mathrm{kmp}}\tilde{a}_1^2(n-m)\tilde{a}_{2\mathrm{est}}^*(n-p)\\ &\times|\tilde{a}_1(n-m)|^{k-1}+e(n)\end{aligned} \tag{45}$$

where

$$\begin{aligned}e(n) = &\sum_{p=0}^{P_1}\beta_p^1\varepsilon(n-p)\\ &+\sum_{k=2}^{K_2}\sum_{m=0}^{M_2}\sum_{p=0}^{P_2}\beta_{\mathrm{kmp}}^2\varepsilon(n-p)|\tilde{a}_1(n-m)|^{k-1}\\ &+\sum_{k=1}^{K_3}\sum_{m=0}^{M_3}\sum_{p=0}^{P_3}\gamma_{\mathrm{kmp}}\tilde{a}_1^2(n-m)\varepsilon^*(n-p)|\tilde{a}_1(n-m)|^{k-1}.\end{aligned} \tag{46}$$

Considering that $\varepsilon(n)=\sum_{q=1}^{Q}\left(d_q/d_0-1\right)\tilde{a}_1(n-q)$, then, (45) can be expressed with only the input signal $\tilde{a}_1(n)$, as in the following equation:

$$\begin{aligned}e(n) = &\sum_{m_1=1}^{P_1+Q}\theta_{m_1}^1\tilde{a}_1(n-m_1)\\ &+\sum_{k=2}^{K_2}\sum_{m=0}^{M_2}\sum_{m_2=1}^{P_2+Q}\theta_{k,m,m_2}^2\tilde{a}_1(n-m_2)|\tilde{a}_1(n-m)|^{k-1}\\ &+\sum_{k=1}^{K_3}\sum_{m=0}^{M_3}\sum_{m_3=1}^{P_3+Q}\theta_{k,m,m_3}^3\tilde{a}_1^2(n-m)\tilde{a}_1^*(n-m_3)\\ &\times|\tilde{a}_1(n-m)|^{k-1}\end{aligned} \tag{47}$$

where $\theta_{m_1}^1$, θ_{k,m,m_2}^2, and θ_{k,m,m_3}^3 denote the recombined coefficients, which have the form as

$$\theta_{m_1}^1=\sum_{p=0}^{P_1}\sum_{q=1}^{Q}\beta_p^1\left(d_q/d_0-1\right),\quad\text{s.t.}\quad m_1=p+q$$

$$\theta_{k,m,m_2}^2=\sum_{p=0}^{P_2}\sum_{q=1}^{Q}\beta_{\mathrm{kmp}}^2\left(d_q/d_0-1\right),\quad\text{s.t.}\quad m_2=p+q$$

$$\theta_{k,m,m_3}^3=\sum_{p=0}^{P_2}\sum_{q=1}^{Q}\gamma_{\mathrm{kmp}}\left(d_q/d_0-1\right)^*,\quad\text{s.t.}\quad m_3=p+q.$$

As it can be seen, the polynomial terms with aligned memory index can be absorbed in the first term group in (45) by altering the memory depth M_1 and model coefficients α_{km}. As for the remaining nonlinear terms with cross-memory index, their contributions to the nonlinearity of the output signal $\tilde{b}_{2\mathrm{act}}(n)$ are usually less significant compared to the aligned memory and static nonlinear terms. Considering the tradeoff between the complexity and modeling accuracy, the performance degradation would be acceptable if we ignore these terms in application scenarios for mobile handsets where power consumption budgets for DPD resources are limited.

In such a case, although the reflection signal $\tilde{a}_2(n)$ is approximated by (26), the form and composition of the TD-PHD model remain unchanged, and the LMT-DPD technique will still be effective. Note that the estimation in (26) is valid only if parameter Q is within an appropriate range. For example, parameter Q is selected within 2–5 in our measurements for both stability and accuracy.

REFERENCES

[1] B. Kim, I. Kim, and J. Moon, "Advanced Doherty architecture," *IEEE Microw. Mag.*, vol. 11, no. 5, pp. 72–86, Aug. 2010.

[2] P. Gandotra, R. K. Jha, and S. Jain, "Green communication in next generation cellular networks: A survey," *IEEE Access*, vol. 5, pp. 11727–11758, 2017.

[3] A. Katz, J. Wood, and D. Chokola, "The evolution of PA linearization: From classic feedforward and feedback through analog and digital predistortion," *IEEE Microw. Mag.*, vol. 17, no. 2, pp. 32–40, Feb. 2016.

[4] L. Guan and A. Zhu, "Green communications: Digital predistortion for wideband RF power amplifiers," *IEEE Microw. Mag.*, vol. 15, no. 7, pp. 84–99, Nov./Dec. 2014.

[5] F. M. Ghannouchi and O. Hammi, "Behavioral modeling and predistortion," *IEEE Microw. Mag.*, vol. 10, no. 7, pp. 52–64, Dec. 2009.

[6] H. Wang, J. Bao, and Z. Wu, "Comparison of the behavioral modelings for RF power amplifier with memory effects," *IEEE Microw. Wireless Compon. Lett.*, vol. 19, no. 3, pp. 179–181, Mar. 2009.

[7] W. Chen, X. Liu, J. Chu, H. Wu, Z. Feng, and F. M. Ghannouchi, "A low complexity moving average nested GMP model for digital predistortion of broadband power amplifiers," *IEEE Trans. Circuits Syst. I, Reg. Papers*, vol. 69, no. 5, pp. 2070–2083, May 2022.

[8] L. Ding et al., "A robust digital baseband predistorter constructed using memory polynomials," *IEEE Trans. Microw. Theory Techn.*, vol. 52, no. 1, pp. 159–165, Jan. 2004.

[9] W.-J. Kim, S. P. Stapleton, J. H. Kim, and C. Edelman, "Digital predistortion linearizes wireless power amplifiers," *IEEE Microw. Mag.*, vol. 6, no. 3, pp. 54–61, Sep. 2005.

[10] A. Abdelhafiz, L. Behjat, F. M. Ghannouchi, M. Helaoui, and O. Hammi, "A high-performance complexity reduced behavioral model and digital predistorter for MIMO systems with crosstalk," *IEEE Trans. Commun.*, vol. 64, no. 5, pp. 1996–2004, May 2016.

[11] X. Liu et al., "Beam-oriented digital predistortion for 5G massive MIMO hybrid beamforming transmitters," *IEEE Trans. Microw. Theory Techn.*, vol. 66, no. 7, pp. 3419–3432, Jul. 2018.

[12] Y. Li, W. Cao, and A. Zhu, "Instantaneous sample indexed magnitude-selective affine function-based behavioral model for digital predistortion of RF power amplifiers," *IEEE Trans. Microw. Theory Techn.*, vol. 66, no. 11, pp. 5000–5010, Nov. 2018.

[13] W. Cao and A. Zhu, "A modified decomposed vector rotation-based behavioral model with efficient hardware implementation for digital predistortion of RF power amplifiers," *IEEE Trans. Microw. Theory Techn.*, vol. 65, no. 7, pp. 2443–2452, Jul. 2017.

[14] D. Ji, J. Jeon, and J. Kim, "A novel load mismatch detection and correction technique for 3G/4G load insensitive power amplifier application," *IEEE Trans. Microw. Theory Techn.*, vol. 63, no. 5, pp. 1530–1543, May 2015.

[15] D. Ji, J. Jeon, and J. Kim, "A novel load insensitive RF power amplifier using a load mismatch detection and curing technique," in *Proc. IEEE Radio Freq. Integr. Circuits Symp. (RFIC)*, Jun. 2013, pp. 341–344.

[16] S. K. Dhar, A. Abdelhafiz, M. Aziz, M. Helaoui, and F. M. Ghannouchi, "A reflection-aware unified modeling and linearization approach for power amplifier under mismatch and mutual coupling," *IEEE Trans. Microw. Theory Techn.*, vol. 66, no. 9, pp. 4147–4157, Sep. 2018.

[17] A. Keerti and A.-V. H. Pham, "RF characterization of SiGe HBT power amplifiers under load mismatch," *IEEE Trans. Microw. Theory Techn.*, vol. 55, no. 2, pp. 207–214, Feb. 2007.

[18] J. Ponte, A. Ghahremani, M. Huiskamp, A.-J. Annema, and B. Nauta, "Augmentation of Class-E PA reliability under load mismatch conditions," in *Proc. 25th IEEE Int. Conf. Electron., Circuits Syst. (ICECS)*, Dec. 2018, pp. 33–36.

[19] W. Fei, J. Su, G. Tingming, L. Jun, and S. Lingling, "RF characterization of GaAs HBT under load mismatch with real-time load-pull system," in *IEEE MTT-S Int. Microw. Symp. Dig.*, Sep. 2020, pp. 1–3.

[20] X. Mu, Z. Alon, G. Zhang, and S. Chang, "Analysis of output power variation under mismatched load in power amplifier FEM with directional coupler," in *IEEE MTT-S Int. Microw. Symp. Dig.*, Jun. 2009, pp. 549–552.

[21] A. Ghahremani, A.-J. Annema, and B. Nauta, "Load mismatch sensitivity of class-E power amplifiers," *IEEE Trans. Microw. Theory Techn.*, vol. 67, no. 1, pp. 216–230, Jan. 2019.

[22] S. Sinha, C. V. N. Rao, and D. Pujara, "Balanced power amplifier protection against load mismatch," *IEEE Microw. Wireless Compon. Lett.*, vol. 28, no. 2, pp. 165–167, Feb. 2018.

[23] H. Lyu and K. Chen, "Balanced-to-Doherty mode-reconfigurable power amplifier with high efficiency and linearity against load mismatch," *IEEE Trans. Microw. Theory Techn.*, vol. 68, no. 5, pp. 1717–1728, May 2020.

[24] R. Quaglia, J. R. Powell, K. A. Chaudhry, and S. C. Cripps, "Mitigation of load mismatch effects using an orthogonal load modulated balanced amplifier," *IEEE Trans. Microw. Theory Techn.*, vol. 70, no. 6, pp. 3329–3341, Jun. 2022.

[25] R. Argaez-Ramirez, J.-R. Perez-Cisneros, and C. Fager, "Investigation of power amplifier performance under load mismatch conditions," in *Proc. IEEE Topical Conf. RF/Microwave Power Model. Radio Wireless Appl. (PAWR)*, Jan. 2021, pp. 41–43.

[26] C. D. Presti, D. F. Kimball, and P. M. Asbeck, "Closed-loop digital predistortion system with fast real-time adaptation applied to a handset WCDMA PA module," *IEEE Trans. Microw. Theory Techn.*, vol. 60, no. 3, pp. 604–618, Mar. 2012.

[27] H. Zargar, A. Banai, and J. C. Pedro, "A new double input-double output complex envelope amplifier behavioral model taking into account source and load mismatch effects," *IEEE Trans. Microw. Theory Techn.*, vol. 63, no. 2, pp. 766–774, Feb. 2015.

[28] J. Cai, R. Goncalves, and J. C. Pedro, "A new complex envelope behavioral model for load mismatched power amplifiers," *Int. J. RF Microw. Comput.-Aided Eng.*, vol. 27, no. 6, pp. 1–9, 2017.

[29] F. M. Barradas, T. R. Cunha, P. M. Cabral, and J. C. Pedro, "Modeling PA linearity and efficiency in MIMO transmitters," in *IEEE MTT-S Int. Microw. Symp. Dig.*, Jun. 2017, pp. 1999–2002.

[30] F. M. Barradas, P. M. Tomé, J. M. Gomes, T. R. Cunha, P. M. Cabral, and J. C. Pedro, "Power, linearity, and efficiency prediction for MIMO arrays with antenna coupling," *IEEE Trans. Microw. Theory Techn.*, vol. 65, no. 12, pp. 5284–5297, Dec. 2017.

[31] C. Fager, X. Bland, K. Hausmair, J. C. Cahuana, and T. Eriksson, "Prediction of smart antenna transmitter characteristics using a new behavioral modeling approach," in *IEEE MTT-S Int. Microw. Symp. Dig.*, Jun. 2014, pp. 1–4.

[32] K. Hausmair et al., "Prediction of nonlinear distortion in wideband active antenna arrays," *IEEE Trans. Microw. Theory Techn.*, vol. 65, no. 11, pp. 4550–4563, Nov. 2017.

[33] Z. Dunn, M. Yeary, C. Fulton, and R. Rincon, "Impedance-dependent wideband digital predistortion of solid-state radar amplifiers," *IEEE Trans. Aerosp. Electron. Syst.*, vol. 53, no. 5, pp. 2290–2303, Oct. 2017.

[34] X. Wang, Y. Li, and A. Zhu, "Digital predistortion using extended Magnitude- selective affine functions for 5G handset power amplifiers with load mismatch," *IEEE Trans. Microw. Theory Techn.*, vol. 70, no. 5, pp. 2825–2834, May 2022.

[35] X. Liu, W. Chen, W. Chen, Y. Guo, and Z. Feng, "Load-mismatch tracking digital predistortion for mobile-terminal power amplifiers," in *IEEE MTT-S Int. Microw. Symp. Dig.*, Denver, CO, USA, Jun. 2022, pp. 506–509.

[36] J. Verspecht and D. E. Root, "Polyharmonic distortion modeling," *IEEE Microw. Mag.*, vol. 7, no. 3, pp. 44–57, Jun. 2006.

[37] D. E. Root, J. Verspecht, D. Sharrit, J. Wood, and A. Cognata, "Broadband poly-harmonic distortion (PHD) behavioral models from fast automated simulations and large-signal vectorial network measurements," *IEEE Trans. Microw. Theory Techn.*, vol. 53, no. 11, pp. 3656–3664, Nov. 2005.

[38] K. R. Boyle, E. Spits, M. A. de Jongh, S. Sato, T. Bakker, and A. van Bezooijen, "A self-contained adaptive antenna tuner for mobile phones: Featuring a self-learning calibration procedure," in *Proc. 6th Eur. Conf. Antennas Propag. (EUCAP)*, Mar. 2012, pp. 1804–1808.

[39] V. Solomko, R. Bauder, and A. Thomas, "Successive approximation RF reflectometer for antenna tuning in cellular handheld devices," *IEEE Trans. Circuits Syst. I, Reg. Papers*, vol. 65, no. 5, pp. 1731–1743, May 2018.

[40] L. Sankey and Z. Popovic, "Adaptive tuning for handheld transmitters," in *IEEE MTT-S Int. Microw. Symp. Dig.*, Jun. 2009, pp. 225–228.

[41] K. Hausmair, P. N. Landin, U. Gustavsson, C. Fager, and T. Eriksson, "Digital predistortion for multi-antenna transmitters affected by antenna crosstalk," *IEEE Trans. Microw. Theory Techn.*, vol. 66, no. 3, pp. 1524–1535, Mar. 2018.

[42] Q. Luo, X. Zhu, C. Yu, and W. Hong, "Single-receiver over-the-air digital predistortion for massive MIMO transmitters with antenna crosstalk," *IEEE Trans. Microw. Theory Techn.*, vol. 68, no. 1, pp. 301–315, Jan. 2020.

[43] Z. Wang, W. Chen, G. Su, F. M. Ghannouchi, Z. Feng, and Y. Liu, "Low computational complexity digital predistortion based on direct learning with covariance matrix," *IEEE Trans. Microw. Theory Techn.*, vol. 65, no. 11, pp. 4274–4284, Nov. 2017.

[44] D. R. Morgan, Z. Ma, J. Kim, M. G. Zierdt, and J. Pastalan, "A generalized memory polynomial model for digital predistortion of RF power amplifiers," *IEEE Trans. Signal Process.*, vol. 54, no. 10, pp. 3852–3860, Oct. 2006.

Xin Liu (Member, IEEE) received the B.S. degree in electronic information science and technology from Xidian University, Xi'an, China, in 2017, and the Ph.D. degree in electronic engineering from Tsinghua University, Beijing, China, in 2022.

She is currently an Associate Professor with the Key Laboratory of Wide Bandgap Semiconductor Technology, School of Microelectronics, Xidian University. Her current research interests include the radio frequency (RF) power amplifier, digital predistortion, and linearization techniques for RF transmitters.

Dr. Liu was a recipient of the IEEE Microwave Theory and Technology Society (MTT-S) Graduate Fellowship Award in 2021.

Wenhua Chen (Senior Member, IEEE) received the B.S. degree in microwave engineering from the University of Electronic Science and Technology of China (UESTC), Chengdu, China, in 2001, and the Ph.D. degree in electronic engineering from Tsinghua University, Beijing, China, in 2006.

From 2010 to 2011, he was a Post-Doctoral Fellow with the iRadio Laboratory, University of Calgary, Calgary, AB, Canada. He is currently a Professor with the Department of Electronic Engineering, Tsinghua University. He has authored or coauthored over 200 journal articles and conference papers. His main research interests include energy-efficient power amplifier (PA) and linearization, and millimeter-wave integrated circuits.

Dr. Chen was a recipient of the Outstanding Youth Science Foundation of National Natural Science Foundation of China (NSFC) in 2015, the Union Radio-Scientifique Internationale (URSI) Young Scientist Award in 2014, and the student paper awards at several international conferences. He was an Associate Editor of the IEEE TRANSACTIONS ON MICROWAVE THEORY AND TECHNIQUES. He is also an Associate Editor of IEEE MICROWAVE AND WIRELESS COMPONENTS LETTERS and an Editorial Member of *Engineering*.

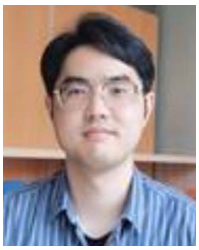

Wenhao Chen received the B.S. degree in communication engineering from the East China University of Science and Technology, Shanghai, China, in 2013, and the Ph.D. degree in communication engineering from the University of Chinese Academy of Sciences, Beijing, China, in 2019.

He is currently a Senior Research Engineer with the Wireless Terminal Chipset Algorithm Development Department, Huawei Hisilicon, Shanghai. His current research interests include array signal processing, digital predistortion, and sparse signal processing for compact wireless transmitters.

Yan Guo received the B.E. degree in information science and engineering from East China Jiaotong University, Nanchang, Jiangxi, China, in 2007, the M.E. degree in communication and information systems from Southeast University, Nanjing, China, in 2011, and the Ph.D. degree in electronic engineering from University College Dublin (UCD), Dublin, Ireland, in 2016.

He is currently a Digital Front-End Expert and a Research Team Leader with the Wireless Terminal Chipset Algorithm Department, Huawei Hisilicon, Shanghai, China. His main research interests include digital predistortion, wideband envelope tracking PA linearization, array signal processing, and artificial intelligence (AI)-assisted radio frequency (RF) signal processing for compact wireless transmitters.

Zhenghe Feng (Life Fellow, IEEE) received the B.S. degree in radio and electronics from Tsinghua University, Beijing, China, in 1970.

Since 1970, he has been with Tsinghua University as an Assistant, a Lecturer, an Associate Professor, and a Full Professor. His main research areas include numerical techniques and computational electromagnetics, radio frequency (RF) and microwave circuits and antenna, wireless communications, smart antenna, and spatial–temporal signal processing.